

# The ultrafast Einstein–de Haas effect

C. Dornes<sup>1\*</sup>, Y. Acremann<sup>2</sup>, M. Savoini<sup>1</sup>, M. Kubli<sup>1</sup>, M. J. Neugebauer<sup>1</sup>, E. Abreu<sup>1</sup>, L. Huber<sup>1</sup>, G. Lantz<sup>1</sup>, C. A. F. Vaz<sup>3</sup>, H. Lemke<sup>4</sup>, E. M. Bothschafter<sup>3</sup>, M. Porer<sup>3</sup>, V. Esposito<sup>3</sup>, L. Rettig<sup>3,5</sup>, M. Buzzi<sup>3,6</sup>, A. Alberca<sup>3</sup>, Y. W. Windsor<sup>3,5</sup>, P. Beaud<sup>4</sup>, U. Staub<sup>3</sup>, Diling Zhu<sup>7</sup>, Sanghoon Song<sup>7</sup>, J. M. Glownia<sup>7</sup> & S. L. Johnson<sup>1,4\*</sup>

The Einstein–de Haas effect was originally observed in a landmark experiment<sup>1</sup> demonstrating that the angular momentum associated with aligned electron spins in a ferromagnet can be converted to mechanical angular momentum by reversing the direction of magnetization using an external magnetic field. A related problem concerns the timescale of this angular momentum transfer. Experiments have established that intense photoexcitation in several metallic ferromagnets leads to a drop in magnetization on a timescale shorter than 100 femtoseconds—a phenomenon called ultrafast demagnetization<sup>2–4</sup>. Although the microscopic mechanism for this process has been hotly debated, the key question of where the angular momentum goes on these femtosecond timescales remains unanswered. Here we use femtosecond time-resolved X-ray diffraction to show that most of the angular momentum lost from the spin system upon laser-induced demagnetization of ferromagnetic iron is transferred to the lattice on sub-picosecond timescales, launching a transverse strain wave that propagates from the surface into the bulk. By fitting a simple model of the X-ray data to simulations and optical data, we estimate that the angular momentum transfer occurs on a timescale of 200 femtoseconds and corresponds to 80 per cent of the angular momentum that is lost from the spin system. Our results show that interaction with the lattice has an essential role in the process of ultrafast demagnetization in this system.

Proposed mechanisms for ultrafast demagnetization generally fall into two categories: spin-flip scattering and spin-transport mechanisms. The first category explains the demagnetization process as a sudden increase in scattering processes that ultimately result in a decrease of spin order. These scattering processes can include electron–electron, electron–phonon, electron–magnon and even direct spin–light interactions. On average, such scattering must involve a transfer of angular momentum from the electronic spins to one or more other subsystems. Candidates include the lattice, the electromagnetic field and the orbital angular momentum of the electrons. Numerical estimates and experiments using circularly polarized light strongly suggest that the amount of angular momentum given to the electromagnetic field interaction is negligible<sup>5</sup>, and experiments using femtosecond X-ray magnetic circular dichroism indicate that the angular momenta of electronic spins and orbitals decrease in magnitude nearly simultaneously<sup>6–8</sup>. Therefore, the only remaining possibility for a spin-flip-induced change in angular momentum appears to be a transfer to the lattice via spin–orbit coupling<sup>9</sup>. Recent theoretical *ab initio* studies support this view<sup>10–12</sup>, but it remains to be experimentally verified.

The second category of proposed mechanisms relies on the idea that laser excitation causes a rapid transport of majority spins away from the excited region. Transport is considerably less efficient for minority spins, leaving behind a region of reduced magnetization density<sup>13</sup>. This mechanism has recently been investigated experimentally. One experiment has observed indirect demagnetization of ferromagnets by photoexciting a neighbouring metallic layer<sup>14,15</sup>, whereas other

groups have reported spin injection from a photoexcited ferromagnetic layer into a deeper-lying, unpumped layer of another ferromagnetic or nonmagnetic metal<sup>16,17</sup>. If we consider the demagnetization process as a result of spin transport alone, the angular momentum of the entire system remains in the spin subsystem. In this case, the observed demagnetization is interpreted as a local effect, arising from the laser-induced spatial inhomogeneity. By contrast, studies have found sizeable ultrafast demagnetization of thin ferromagnetic films on insulating substrates<sup>18</sup>. In a transport model, it is hard to explain an

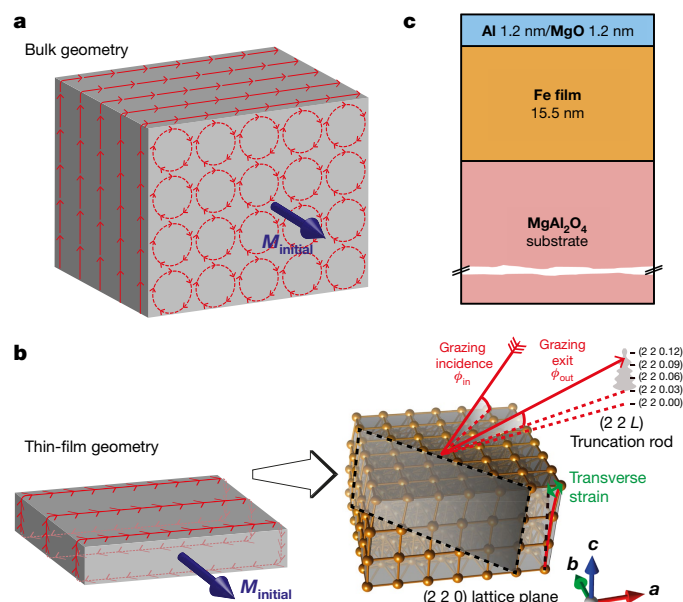


**Fig. 1 | Overview of the experiment and its implementation.** **a**, Thought experiment of the ultrafast Einstein–De Haas effect. A bulk ferromagnet has initial magnetisation  $M_{\text{initial}}$ , indicated by the blue arrow. After a spatially uniform partial demagnetization, the demagnetized subunits of the bulk exert a spatially uniform torque (dashed red circles). The forces from these internal torques cancel everywhere except at surfaces with normals not parallel to  $M_{\text{initial}}$ , resulting in a transverse force (indicated by the red solid arrows). **b**, Ultrafast Einstein–De Haas effect in a thin-film sample (left) and the actual geometry for our X-ray diffraction experiment (right). In the left panel, the red arrows indicate transverse forces on the surface, which arise from the transfer of angular momentum. In the right panel, the direction of the incoming and outgoing X-ray beams are indicated with thick red arrows. The incoming angle  $\varphi_{\text{in}}$  is fixed, while there is a range of outgoing angles  $\varphi_{\text{out}}$  simultaneously, as given by the crystal truncation rod. This is indicated by the grey shading on the outgoing side. The two dashed red lines show the nominal outgoing beam directions for the (2 2 0) Bragg peak and the geometric horizon of the sample, respectively. The dashed rectangle indicates the (2 2 0) lattice plane. **c**, Layer structure of the thin-film sample used in the experiment.

<sup>1</sup>Institute for Quantum Electronics, Physics Department, ETH Zurich, Zurich, Switzerland. <sup>2</sup>Laboratory for Solid State Physics, Physics Department, ETH Zurich, Zurich, Switzerland. <sup>3</sup>Swiss Light Source, Paul Scherrer Institute, Villigen, Switzerland. <sup>4</sup>SwissFEL, Paul Scherrer Institute, Villigen, Switzerland. <sup>5</sup>Fritz Haber Institute of the Max Planck Society, Berlin, Germany. <sup>6</sup>Max Planck Institute for the Structure and Dynamics of Matter, Hamburg, Germany. <sup>7</sup>Linac Coherent Light Source (LCLS), SLAC National Accelerator Laboratory, Menlo Park, CA, USA. \*e-mail: dornesc@phys.ethz.ch; johnson@phys.ethz.ch

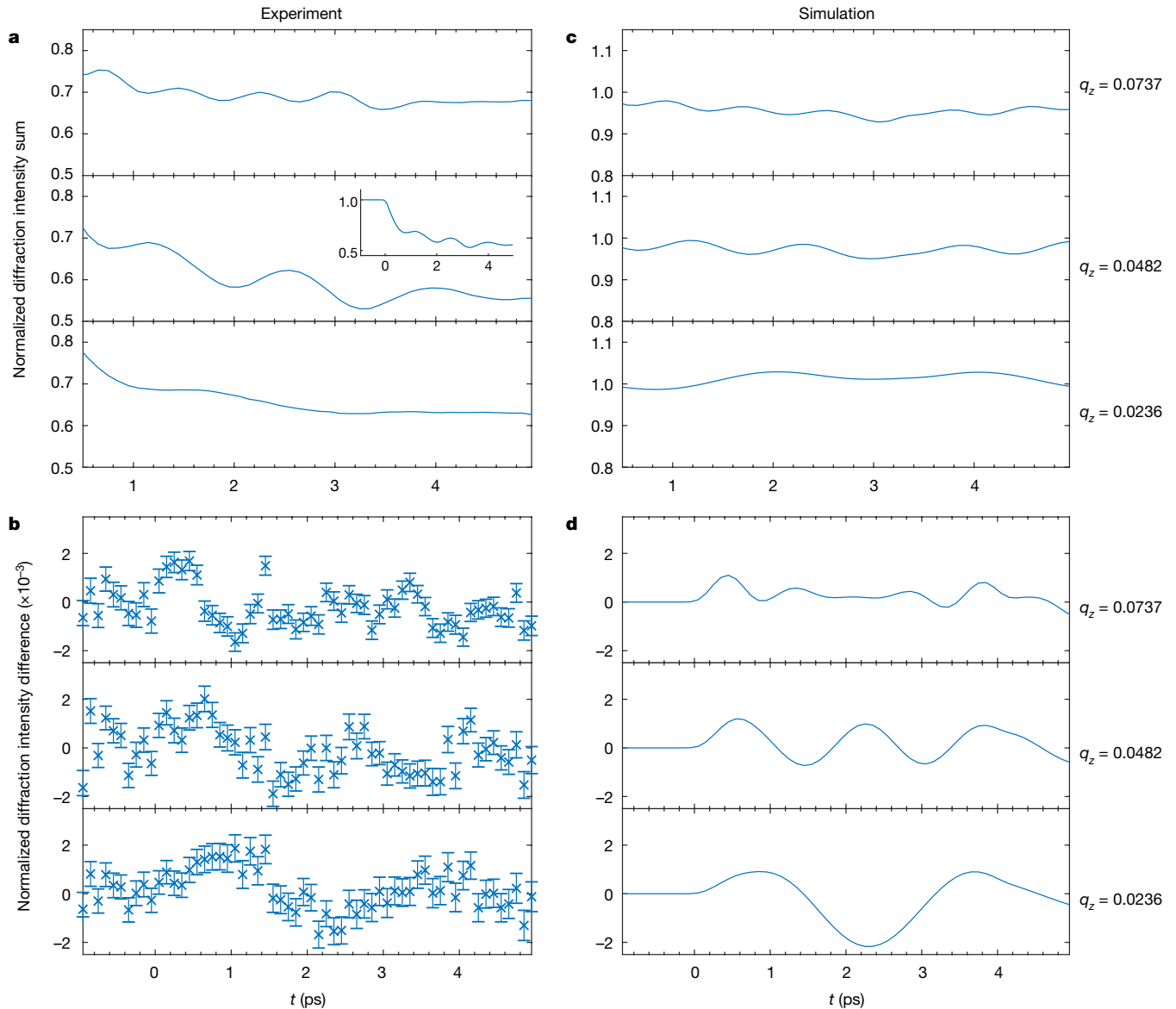


**Fig. 2 | Time-resolved X-ray diffraction signal, measured and simulated at different values of the out-of-plane momentum transfer  $q_z$ .** The central values of the three  $q_z$  bands, in reciprocal lattice units, are shown on the right side of the plot. **a, b**, Experimental data. **c, d**, Best-fitting simulated data (absolute demagnetization,  $\Delta M/M = 0.08$ ; angular momentum transfer time, 200 fs). The plots in **a** and **c** show the experimental (**a**) and simulated (**c**) sum of the intensities measured in the two magnetization directions, normalized to the value measured before laser excitation at each  $q_z$ . For the experimental data in **a**, the error bars

are comparable to the line thickness and have been omitted for clarity. The inset shows the full time and intensity range to illustrate the initial intensity drop due to the onset of thermal disorder (Debye–Waller factor). Panels **b** and **d** show the experimental (**b**) and simulated (**d**) difference between the diffraction intensities measured in antiparallel magnetization directions, normalized to the sum of these intensities for the different values of  $q_z$ . The error bars in **b** represent the standard error of the mean from 158 independent scans.

almost unchanged demagnetization process when the large bandgap of the substrate blocks the transport of carriers away from the excited region. From this, it appears that although spin transport can contribute to ultrafast demagnetization, there must also be sizeable contributions from spin-flip scattering.

If indeed some fraction of angular momentum is transferred to the crystal lattice on ultrafast timescales, it should be possible to quantitatively measure the resulting structural dynamics. The dynamics of the Einstein–de Haas effect have been previously considered in other contexts<sup>19,20</sup>. Here we consider specifically the case in which bulk, magnetized iron is uniformly demagnetized by a homogeneous femtosecond pump excitation. The idea is illustrated in Fig. 1a. Sudden demagnetization causes mechanical torques that lead to unbalanced forces on the surfaces but not inside the bulk. We postulate that ultrafast demagnetization causes a transient volume torque density  $\boldsymbol{\tau} = -\gamma^{-1}d\mathbf{M}/dt$ ,

where  $\mathbf{M}$  is the initial magnetization,  $t$  is the time and  $\gamma$  is the gyromagnetic ratio<sup>1</sup>. The latter is often expressed using the dimensionless magnetomechanical factor  $g' = -\gamma\hbar/\mu_B$  (where  $\hbar$  is the reduced Planck constant and  $\mu_B$  is the Bohr magneton), which is related, but not identical, to the spectroscopic  $g$  factor<sup>21,22</sup>. In a continuum model of lattice dynamics, a torque density  $\boldsymbol{\tau}$  contributes to the off-diagonal elements of an antisymmetric stress tensor  $\sigma^M$  as  $\sigma_{12}^M = -\sigma_{21}^M = \tau_3$ ,  $\sigma_{23}^M = -\sigma_{32}^M = \tau_1$  and  $\sigma_{31}^M = -\sigma_{13}^M = \tau_2$ . The resulting structural dynamics can be found by using the equation of motion

$$\rho \frac{\partial^2 u_i}{\partial t^2} = \sum_j \frac{\partial \sigma_{ij}}{\partial x_j} \quad (1)$$

where  $\rho$  is the mass density of the material,  $u_i$  (with  $i = 1, 2, 3$ ) are components of the displacement,  $x_i$  are Cartesian coordinates and

$\sigma_{ij}$  are components of the full stress tensor. The stress tensor can be written as

$$\sigma_{ij} = \sum_{kl} C_{ijkl} \eta_{kl} + \sigma_{ij}^M + \sigma_{ij}^{(\text{ext})} \quad (2)$$

where  $C_{ijkl}$  are the elastic constants,  $\eta_{ij} = \frac{1}{2} \left( \frac{\partial u_i}{\partial x_j} + \frac{\partial u_j}{\partial x_i} \right)$  is the strain and  $\sigma_{ij}^{(\text{ext})}$  are the components of any other applied stresses (for example, expansive stress from heating, or magnetostriction) that do not constitute a torque density. Because equation (1) contains only spatial derivatives of the stress, we expect the largest structural displacements caused by angular momentum transfer to begin where the gradient in the absolute demagnetization is the largest; for example, at interfaces. As an illustrative example let us consider the uniform demagnetization of a free-standing thin iron film with surfaces normal to the  $x_3$  direction. The film is initially magnetized to saturation in the  $x_1$  direction, as shown in Fig. 1b. We assume that initially there is no strain in the film. For now we also ignore effects such as thermal expansion, which would contribute to diagonal components of  $\sigma^{(\text{ext})}$ . Under these assumptions, the only non-zero contributions in equation (2) are due to  $\sigma_{23}^M = -\sigma_{32}^M = -\gamma^{-1} dM/dt$ . This implies that in the interior of the film the stress is uniform, with no immediate acceleration of the displacement. At the free surfaces of the film we have the boundary condition

$$\sigma_{3j} = 0 \quad (3)$$

which implies

$$\sum_{kl} C_{32kl} \eta_{kl} = -\frac{1}{\gamma} \frac{dM}{dt} \quad (4)$$

In  $\alpha$ -iron, the only non-zero components of the left-hand side of equation (4) involve  $C_{3223}$ , leading to

$$\eta_{23} = -\frac{1}{2\gamma C_{3232}} \frac{dM}{dt} \quad (5)$$

at the two surfaces. Solving equation (1) yields an impulsive transverse strain wave that propagates into the film from the interfaces. The duration of strain-wave generation is the timescale over which the angular momentum transfer occurs. The amplitude of the transverse wave is proportional to the magnitude of the mechanical torque from the demagnetization process and, consequently, the angular momentum transfer to the lattice. Expansive stresses from heating produce a similar effect via the diagonal elements of  $\sigma^{(\text{ext})}$ , but drive a longitudinal strain wave propagating from the interfaces, as has been well established in ultrafast acoustics<sup>23</sup>.

In our experiment we performed time-resolved X-ray diffraction measurements of these structural dynamics using a magnetic iron film. As illustrated in Fig. 1c, instead of a free-standing film we used a single-crystal iron film grown epitaxially on a non-magnetic  $\text{MgAl}_2\text{O}_4$  substrate with thin capping layers of MgO and Al. The film was initially magnetized in-plane by an applied magnetic field and was then partially demagnetized by an ultrafast laser pulse with a wavelength of 800 nm and duration of 40 fs. To measure the lattice dynamics with a high sensitivity to transverse strain, we performed grazing-incidence diffraction close to the in-plane (2 2 0) reflection. Using an X-ray area detector, we mapped the intensity along its (2 2 L) crystal truncation rod as a function of time after excitation. This intensity is directly related to the magnitude of the Fourier transform of the lattice displacements and offers a direct measure of both transverse and longitudinal strain<sup>24</sup>.

Figure 2 shows the data for selected values of the X-ray momentum transfer along the truncation rod alongside the results of simulations using a discrete lattice dynamics model (see Methods). To identify dynamics that are connected to  $\sigma^M$ , we performed measurements for opposite directions of the initial magnetization and subtracted the resulting data—a procedure that removes all contributions that do not depend on the sign of  $dM/dt$ . We see clear oscillations in this difference

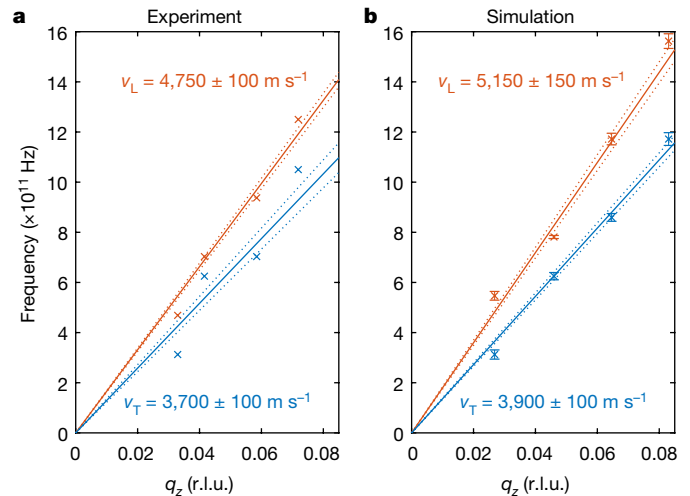


**Fig. 3 | Frequency of modulations observed in the X-ray diffraction signal as a function of the out-of-plane momentum transfer  $q_z$ .**

**a, b**, Experimental results (**a**) and results of simulated datasets analysed in the same way as the experimental data (**b**; see Methods). The red data points are derived from a fast Fourier transform analysis of data resulting from summing intensities measured in the two opposite magnetization directions, whereas the blue data points are derived from the corresponding subtraction (see Methods for details). The solid lines show fits of the general form  $\omega = vq_z$ , and the  $1\sigma$  confidence intervals of the fits are indicated with dashed lines. Both experimental and simulation results show a different slope  $v$  for the sum and difference data, with values that are consistent with the speed of sound for longitudinal and transverse acoustic waves, respectively (r.l.u., reciprocal lattice units). The error bars in **b** are the asymptotic errors from a Gaussian peak fit to fast Fourier transforms of the simulated data at the selected values of the momentum transfer (see Methods).

signal (Fig. 2b), which correspond closely to the expectations from our simulations. This is direct evidence of angular momentum transfer to the lattice on sub-picosecond timescales. For comparison, Fig. 2a also shows the dynamics for the sum of data obtained using opposite initial magnetizations. These data show a drop in intensity (see inset in Fig. 2a), as well as oscillations at a slightly higher frequency. The overall drop in intensity is probably an effect of a strong increase in thermal disorder<sup>25</sup>, which is not directly modelled in our simulations. The oscillation period is that of longitudinal vibrational modes with a wavevector corresponding to the momentum transfer  $q_z$  along the rod; this momentum transfer is modelled in the simulations as the result of an isotropic expansive stress activated by laser excitation.

Figure 3 shows the frequency of oscillations as a function of wavevector  $q_z$  for both the sum and difference data. These results confirm the presence of a transverse and a longitudinal strain wave independently of our simulations. As expected, the difference data agree with the linear relationship  $\omega = v_T q$  where the transverse velocity  $v_T = 3,700 \pm 200 \text{ m s}^{-1}$  is close to the literature value of the transverse acoustic branch in the [001] direction<sup>26</sup>,  $3,875 \pm 20 \text{ m s}^{-1}$ . The sum data show agreement with the linear relationship  $\omega = v_L q$  with  $v_L = 4,750 \pm 100 \text{ m s}^{-1}$ , which is consistent with our measurements of the longitudinal sound velocity by time-resolved optical reflectivity ( $4,730 \pm 150 \text{ m s}^{-1}$ ; see Methods).

By fitting the simulations to the data, we can estimate both the timescale and the magnitude of angular momentum transfer to the lattice. The simulated data plotted in Fig. 2 use our best-fit parameters: an angular momentum transfer time of 200 fs and a total angular momentum transfer to the lattice equal to 8% of the total angular momentum initially in the spin system. On the same sample and under the same photoexcitation conditions, we observed a demagnetization of 10% using time-resolved magneto-optic Kerr spectroscopy. These values imply that, according to our best fit, the angular momentum transfer to the lattice due to the ultrafast Einstein–de Haas effect accounts for

80% of the angular momentum lost from the spins owing to the demagnetization process.

Our results show conclusively that ultrafast demagnetization involves a sub-picosecond transfer of angular momentum to the lattice. At the microscopic level, our results provide strong evidence for the importance of spin-flip processes that directly or indirectly result in the emission of phonons. We expect that similar dynamics govern the behaviour of other systems in which an ultrafast change in spin angular momentum is observed, such as Ni or Co, and in ferrimagnetic systems displaying all-optical switching<sup>27–30</sup>, where a rapid reversal of the direction of the magnetic moment is driven by femtosecond optical pulses. In the latter case, in addition to spin transport between magnetic sublattices or different regions of the material, our results indicate that lattice interactions may need to be considered for an adequate description of ultrafast switching processes. A better understanding of the physical mechanisms behind this angular momentum transfer to the lattice can ultimately assist in the search for next-generation materials for all-optical switching in devices.

### Online content

Any methods, additional references, Nature Research reporting summaries, source data, statements of data availability and associated accession codes are available at <https://doi.org/10.1038/s41586-018-0822-7>.

Received: 18 April 2018; Accepted: 17 October 2018;

Published online 2 January 2019.

- Einstein, A. & de Haas, W. J. Experimenteller Nachweis der Ampèreschen Molekularströme. *Verhandl. Deut. Phys. Ges.* **17**, 152–170 (1915).
- Beaurepaire, E., Merle, J., Daunois, A. & Bigot, J. Ultrafast spin dynamics in ferromagnetic nickel. *Phys. Rev. Lett.* **76**, 4250–4253 (1996).
- Carpene, E. et al. Dynamics of electron–magnon interaction and ultrafast demagnetization in thin iron films. *Phys. Rev. B* **78**, 174422 (2008).
- Fähnle, M. et al. Review of ultrafast demagnetization after femtosecond laser pulses: a complex interaction of light with quantum matter. *Am. J. Phys.* **7**, 68–74 (2018).
- Koopmans, B., Kampen, M. V. & Jonge, W. J. M. D. Experimental access to femtosecond spin dynamics. *J. Phys. Condens. Matter* **15**, S723–S736 (2003).
- Stamm, C. et al. Femtosecond modification of electron localization and transfer of angular momentum in nickel. *Nat. Mater.* **6**, 740–743 (2007).
- Stamm, C., Pontius, N., Kachel, T., Wietstruk, M. & Dürr, H. A. Femtosecond X-ray absorption spectroscopy of spin and orbital angular momentum in photoexcited Ni films during ultrafast demagnetization. *Phys. Rev. B* **81**, 104425 (2010).
- Boeglin, C. et al. Distinguishing the ultrafast dynamics of spin and orbital moments in solids. *Nature* **465**, 458–461 (2010).
- Zhang, G. P. & Hübner, W. Laser-induced ultrafast demagnetization in ferromagnetic metals. *Phys. Rev. Lett.* **85**, 3025–3028 (2000).
- Töws, W. & Pastor, G. M. Many-body theory of ultrafast demagnetization and angular momentum transfer in ferromagnetic transition metals. *Phys. Rev. Lett.* **115**, 217204 (2015).
- Krieger, K., Dewhurst, J. K., Elliott, P., Sharma, S. & Gross, E. K. U. Laser-induced demagnetization at ultrashort time scales: predictions of TDDFT. *J. Chem. Theory Comput.* **11**, 4870–4874 (2015).
- Shokeen, V. et al. Spin flips versus spin transport in nonthermal electrons excited by ultrashort optical pulses in transition metals. *Phys. Rev. Lett.* **119**, 107203 (2017).
- Battiato, M., Carva, K. & Oppeneer, P. M. Superdiffusive spin transport as a mechanism of ultrafast demagnetization. *Phys. Rev. Lett.* **105**, 027203 (2010).
- Eschenlohr, A. et al. Ultrafast spin transport as key to femtosecond demagnetization. *Nat. Mater.* **12**, 332–336 (2013).
- Khorsand, A. R., Savoini, M., Kirilyuk, A. & Rasing, T. Optical excitation of thin magnetic layers in multilayer structures. *Nat. Mater.* **13**, 101–102 (2014).
- Turgut, E. et al. Controlling the competition between optically induced ultrafast spin-flip scattering and spin transport in magnetic multilayers. *Phys. Rev. Lett.* **110**, 197201 (2013).

- Melnikov, A. et al. Ultrafast transport of laser-excited spin-polarized carriers in Au/Fe/MgO(001). *Phys. Rev. Lett.* **107**, 076601 (2011).
- Schellekens, A. J., Verhoeven, W., Vader, T. N. & Koopmans, B. Investigating the contribution of superdiffusive transport to ultrafast demagnetization of ferromagnetic thin films. *Appl. Phys. Lett.* **102**, 252408 (2013).
- Jaafar, R., Chudnovsky, E. M. & Garanin, D. A. Dynamics of the Einstein–de Haas effect: application to a magnetic cantilever. *Phys. Rev. B* **79**, 104410 (2009).
- Mentink, J. H., Katsnelson, M. I. & Lemoshko, M. Quantum many-body dynamics of the Einstein–de Haas effect. Preprint at <https://arxiv.org/abs/1802.01638> (2018).
- Kittel, C. On the gyromagnetic ratio and spectroscopic splitting factor of ferromagnetic substances. *Phys. Rev.* **76**, 743–748 (1949).
- Van Vleck, J. H. The theory of ferromagnetic resonance. *Phys. Rev.* **78**, 266–274 (1950).
- Thomsen, C., Grahn, H. T., Maris, H. J. & Tauc, J. Surface generation and detection of phonons by picosecond light pulses. *Phys. Rev. B* **34**, 4129–4138 (1986).
- Macdonald, J. E. X-ray scattering from semiconductor interfaces. *Faraday Discuss. Chem. Soc.* **89**, 191–200 (1990).
- Mohanlal, S. K. An experimental determination of the Debye–Waller factor for iron by neutron diffraction. *J. Phys. C* **12**, L651–L653 (1979).
- Minkiewicz, V. J., Shirane, G. & Nathans, R. Phonon dispersion relation for iron. *Phys. Rev.* **162**, 528–531 (1967).
- Stanciu, C. D. et al. Subpicosecond magnetization reversal across ferrimagnetic compensation points. *Phys. Rev. Lett.* **99**, 217204 (2007).
- Lambert, C.-H. et al. All-optical control of ferromagnetic thin films and nanostructures. *Science* **345**, 1337–1340 (2014).
- Takahashi, Y. K. et al. Accumulative magnetic switching of ultrahigh-density recording media by circularly polarized light. *Phys. Rev. Appl.* **6**, 054004 (2016).
- Granitzka, P. W. et al. Magnetic switching in granular FePt layers promoted by near-field laser enhancement. *Nano Lett.* **17**, 2426–2432 (2017).

**Acknowledgements** Time-resolved X-ray diffraction measurements were carried out at the XPP endstation at LCLS. Use of the Linac Coherent Light Source (LCLS), SLAC National Accelerator Laboratory, is supported by the US Department of Energy, Office of Science, Office of Basic Energy Sciences under contract number DE-AC02-76SF00515. Preparatory static diffraction measurements were performed at the X04SA beamline of the Swiss Light Source. We acknowledge financial support by the NCCR Molecular Ultrafast Science and Technology (NCCR MUST), a research instrument of the Swiss National Science Foundation (SNSF). E.A. acknowledges support from the ETH Zurich Postdoctoral Fellowship Program and from the Marie Curie Actions for People COFUND programme. E.M.B. acknowledges funding from the European Commission's Seventh Framework Programme (FP7/2007–2013) under grant agreement number 290605 (PSI-FELLOW/COFUND). M.P. acknowledges support from NCCR MARVEL, funded by the SNSF.

**Reviewer information** *Nature* thanks P. G. Evans, M. Münzenberg and S. Sharma for their contribution to the peer review of this work.

**Author contributions** C.D. and S.L.J. conceived and designed the experiment. C.A.F.V. performed the sample fabrication. C.D., M.S., M.K., M.J.N., E.A., L.H., E.M.B., M.P., V.E., L.R. and Y.W.W. performed synchrotron measurements to characterize the sample and prior sample candidates. M.B. and C.D. built the electromagnet. Y.A. built and programmed the pulser for the magnet. A.A. assisted C.D. in analysing X-ray reflectivity measurements of sample candidates. M.S., C.A.F.V., L.H., E.A., G.L., H.L., M.B., P.B. and U.S. gave input to C.D. and S.L.J. on the experimental design and during data analysis. C.D., Y.A., M.S., M.K., H.L., E.M.B., M.P., U.S. and S.L.J. performed the experiment with the help of D.Z., S.S. and J.M.G., the LCLS beamline staff. C.D. and S.L.J. wrote the manuscript and all authors contributed to its final version.

**Competing interests** The authors declare no competing interests.

### Additional information

**Extended data** is available for this paper at <https://doi.org/10.1038/s41586-018-0822-7>.

**Reprints and permissions information** is available at <http://www.nature.com/reprints>.

**Correspondence and requests for materials** should be addressed to C.D. or S.L.J.

**Publisher's note:** Springer Nature remains neutral with regard to jurisdictional claims in published maps and institutional affiliations.

## METHODS

**Sample preparation.** A single-crystal iron film with surface normal (0 0 1) was grown by molecular beam epitaxy on a  $\text{MgAl}_2\text{O}_4$  (0 0 1) spinel substrate, capped on the top by nominally 2-nm-thick layers of MgO and Al to prevent oxidation and X-ray damage. The  $a$  and  $b$  in-plane axes of the film were rotated by  $45^\circ$  with respect to the substrate (epitaxial relationship  $\text{Fe}[110] \parallel \text{MgAl}_2\text{O}_4[100]$ ). The high quality of the sample was verified by various methods, including in situ low-energy electron diffraction, synchrotron measurements of the X-ray reflectivity (XRR) and the sample structure (unit-cell parameters and lateral-coherence length), and post-experiment transmission electron microscopy (TEM) nanographs. The TEM nanographs indicated a total thickness of 17.9 nm, whereas the XRR measurements showed an Fe thickness of 15.5 nm with capping layers of 2.3 nm MgO and 2.7 nm Al. Because the XRR fits have considerably less uncertainty on the Fe film thickness compared to that of the thin capping layers, we consider the discrepancy between TEM and XRR to indicate primarily an uncertainty on the thickness of the capping layers in the XRR measurements.

**Transient magneto-optic Kerr effect measurements.** To calibrate the magnitude of the demagnetization of the sample used in the X-ray experiment, we performed transient magneto-optic Kerr effect (MOKE) measurements using another femtosecond laser operating at 800 nm. The beam profile and incidence angle of the pump from the X-ray experiment were reproduced precisely (see Methods section ‘X-ray pump–probe experiment’); the pump repetition rate for the MOKE was 500 Hz and the pulse duration was 100 fs. Extended Data Fig. 1 shows a series of measurements with increasing fluence. We note that the rapid oscillations during the overlap of the pump and probe pulses (0–300 fs; determined by a noncollinear pump–probe geometry) are not indicative of dynamics in the magnetization but arise from artefacts due to the need to replicate the pump conditions of the X-ray experiment<sup>31,32</sup>. For our analysis we used only the magnitude of the pump–probe effect, averaged from 0.4 ps to 0.7 ps delay time. This yielded the calibration line between fluence and demagnetization shown in Extended Data Fig. 2, which was used for the comparison between demagnetization and mechanical angular momentum discussed in the main text. The fluence dependence measurement confirms that the pump laser conditions of the X-ray experiment were still well below the damage threshold (which occurs at about  $12.5 \text{ mJ cm}^{-2}$  and 15% demagnetization) and in the linear regime of the demagnetization–fluence curve.

**Longitudinal sound-speed measurements.** To measure the longitudinal speed of strain waves in our film we performed pump–probe reflectivity measurements similar to those reported by Thomsen et al.<sup>23</sup>. The pump laser had a wavelength of 800 nm, a pulse duration of 40 fs and a repetition rate of 250 kHz. For the probe, a second-harmonic 400-nm beam was generated using a beta barium borate crystal. We measured a time of  $7.2 \pm 0.1$  ps required for the surface-generated acoustic wave to propagate to the substrate–Fe interface and back. We thus estimate a longitudinal sound velocity of  $4,730 \pm 150 \text{ m s}^{-1}$  for iron, where we assume that the wave propagates twice through 15.5 nm of Fe and 2.4 nm of capping material (in agreement with the stack thickness of 17.9 nm measured via TEM). Here we assumed that the capping layers consist of 50% epitaxial MgO with a longitudinal sound velocity<sup>33</sup> of  $9,088 \text{ m s}^{-1}$  along [001] and 50% Al with an isotropic longitudinal sound velocity<sup>34</sup> of  $6,422 \text{ m s}^{-1}$ .

**X-ray pump–probe experiment.** For the time-resolved experiment at the X-ray pump–probe endstation<sup>35</sup> at LCLS, an external magnetic field was used to set the magnetization direction of the film between X-ray shots. This was achieved using a small laminated-core electromagnet driven by a pulser<sup>36</sup> based on insulated-gate bipolar transistor technology. For each shot of the X-ray laser, the sample magnetization direction was set according to a pseudorandom sequence and tagged for the data acquisition system. This prevented possible periodic disturbances, such as the mains frequency leaking into our magnetic difference signal. A nitrogen cryoblower was used during the measurement and the sample was cooled to 200 K; the main reason for cooling was shielding of the sample from X-ray damage in air, which we had encountered during earlier tests at the Swiss Light Source synchrotron.

The sample was mounted vertically; the incoming angle of the X-rays was  $1^\circ$  and the X-ray photon energy was 6.9 keV with a pulse rate of 120 Hz. The total integration time for the measurement was 10 h, during which 158 pump–probe scans were completed (21 scan steps from  $-1$  ps to 5 ps; 600 shots per step). For each X-ray shot we recorded the incident intensity  $I_0$  using a diode that measured backscattering from a window. The average pulse energy from the machine was 1.8 mJ, leading to roughly  $10^9$  photons per shot at the sample after monochromator and beamline losses. The spectral-encoding-based timing tool of the XPP endstation was used to rebinned the data with 100-fs-wide bins<sup>37</sup>. The measured average diffraction data in each bin was then normalized to the average  $I_0$  for the corresponding shots. The outgoing beam was imaged in a grazing-exit geometry using the CSPAD-140k area detector<sup>38</sup>, yielding single-shot measurements of the  $(2\ 2\ L)$  crystal truncation rod (CTR) with an  $L$  range from 0.03 to about 0.1. This range of momentum transfer is restricted on the lower end by the incidence angle of  $1^\circ$  and the absorption inside

the sample. On the upper end, a hard limit was defined by the detector area, but the strong decrease in signal-to-noise ratio with increasing  $L$  resulted in a useful range of up to 0.1. The effective  $q_z$  resolution decreased owing to sample inhomogeneity, geometric and footprint effects, as well as X-ray divergence.

The optical pump beam was delivered by a femtosecond laser working at 800 nm with a pulse duration of 40 fs and a repetition rate of 120 Hz. We set the incidence angle to  $85^\circ$  and made the pump p-polarized. For the fluence calibration, we measured the mode shape of the optical pump beam at the sample position using a charge-coupled device camera. We then recorded the total incident power for different attenuation settings, as well as the power reflected by the sample. We used the Fresnel transfer-matrix method<sup>39</sup> and the known sample structure to calculate the power absorbed and reflected by the Fe layer as a function of the angle of incidence. The optical constants for this procedure were taken from the literature<sup>40,41</sup>; the best fit to our data gave an incident fluence of  $(8.0 \pm 0.3) \text{ mJ cm}^{-2}$  at an angle of  $(85.64 \pm 0.05)^\circ$ , with  $(2.7 \pm 0.1) \text{ mJ cm}^{-2}$  absorbed by the iron film. The uncertainties in the optical constants and thicknesses do not contribute a substantial error for these calculations; instead, the uncertainties in fluence are dominated by our estimate of how well the pump and probe signals overlapped in the X-ray and MOKE measurements.

To obtain the normalized sum and difference data shown in Fig. 2, the data were sorted by the direction of the initial magnetization. The data in Fig. 2a correspond to the average of both magnetization directions, whereas the traces in Fig. 2b were obtained by subtracting the two opposite directions. To ensure that no sizeable residual signal from the sum data was present in the difference data, we performed a control analysis by randomly partitioning the data collected at one magnetization direction into two parts, as shown in Extended Data Fig. 5.

**X-ray detection of surface strain and transverse displacements.** According to the kinematic theory of X-ray diffraction the scattering intensity  $I_s$  for a given momentum transfer  $\mathbf{Q}$  from a crystal with a monatomic basis is

$$\frac{I_s}{I_0} \propto \left| \sum_{\mathbf{R}} f_0 e^{i\mathbf{r}(\mathbf{R}) \cdot \mathbf{Q}} \right|^2 \quad (6)$$

where the sum runs over all equilibrium positions  $\mathbf{R}$  of the atoms, and  $\mathbf{r}(\mathbf{R})$  is an instantaneous position of the atom near  $\mathbf{R}$ . Here  $f_0$  is the atomic scattering factor for the basis atom. If we now write  $\mathbf{r} = \mathbf{R} + \mathbf{u}$  and  $\mathbf{Q} = \mathbf{G} + \mathbf{q}$ , where  $\mathbf{G}$  is a reciprocal lattice vector close to  $\mathbf{Q}$ , we have

$$\frac{I_s}{I_0} \propto |F_0|^2 - 2 \text{Im} \left[ F_0^* f_0 \sum_{\mathbf{R}} (\mathbf{u} \cdot \mathbf{G}) e^{i\mathbf{R} \cdot \mathbf{q}} \right] - 2 \text{Im} \left[ F_0^* f_0 \sum_{\mathbf{R}} (\mathbf{u} \cdot \mathbf{q}) e^{i\mathbf{R} \cdot \mathbf{q}} \right] \quad (7)$$

where we have performed a series expansion of the complex exponential and kept terms up to first order in  $\mathbf{u}$ . Here  $F_0 = \sum_{\mathbf{R}} f_0 e^{i\mathbf{R} \cdot \mathbf{q}}$  is the structure factor in the absence of strain. In our experiment  $\mathbf{G}$  is directed within the surface plane and  $\mathbf{q}$  is directed along the outward surface normal. Let us define the  $z$  axis as the surface normal, and write  $u_i = \mathbf{u} \cdot \mathbf{G}$  as the component of the displacement along  $\mathbf{G}$ . The second term of equation (7) is proportional to the imaginary part of the Fourier transform of  $u_i$  and the third term is proportional to the imaginary part of the Fourier transform of  $u_z q_z$ . For coherent modes these terms correspond to time-oscillating contributions to the X-ray diffraction signal with an amplitude proportional to the appropriate  $q$ -resolved component of the displacement field. The weighting factors are, however, quite different: the signal from the  $u_i$  component is enhanced by a factor of  $G/q_z$ , which in our experiment ranged from 28 to 94 because we were measuring in the  $(2\ 2\ L)$  CTR with a useable  $L$ -range of 0.03–0.1. **Connection of transverse strain to angular momentum.** In the main manuscript we show that an antisymmetric contribution to the stress tensor that is proportional to the time derivative of the magnetization leads to a transverse strain wave from the surface. Our experimental data show the presence of such a wave. Here we argue that our observations cannot be explained by any other known physical effect.

One of the basic theorems of continuum mechanics is that the conservation of mechanical angular momentum implies that the stress tensor in a material is symmetric<sup>42</sup>; in other words,  $\sigma_{ij} = \sigma_{ji}$ . Antisymmetric components of the stress violate this equality and necessarily lead to changes in the mechanical angular momentum. Thus, we can reformulate the question of whether our transverse strain wave is the result of processes that conserve angular momentum to an equivalent question of whether any known physical mechanism that induces a symmetric stress tensor can result in our observation of transverse strain.

We note that in our experiment we subtract data taken at equal and opposite values of the initial magnetization  $\mathbf{M}$ . Thus, to explain our data we need a contribution to the stress tensor that depends on the magnetization or on some time derivative of it. The only previously known mechanism for this (besides the rotational coupling identified with the Einstein–de Haas effect) is magnetostriction, where the stress tensor depends on the instantaneous value of  $\mathbf{M}$  itself. Because

ferromagnetic  $\alpha$ -iron has inversion symmetry, the magnetostrictive stress depends on  $M$  only through terms that are even in  $M$ . Therefore, any magnetostriction component is subtracted from the signal in our data analysis.

Even if small systematic errors in the magnetization reversal were to lead to a small magnetostrictive contribution to our signal, the stress would follow the temporal dynamics of the magnetization  $M(t)$  and show a step-like behaviour over our measurement window. The resulting dynamics, when resolved in momentum space, would have a cosine-like phase similar to what we see in the longitudinal strain dynamics. In our experiment we observe clearly a sine-like phase in the oscillations, indicating that the stress inducing the dynamics lasts for a short time compared with the period of the Fourier components that we see in our experiment.

Other known methods for generating transverse strain from laser heating<sup>43</sup> rely on anisotropic materials or textured polycrystals, which do not apply to the present situation. In addition, these mechanisms are also independent of the sign of the magnetization and would all lead to cosine-like oscillations. Finally, one could also imagine that transverse strain is generated by the substrate or the neighbouring capping layer. These materials are, however, optically transparent, inversion-symmetric and nonmagnetic. It is therefore difficult to see how the pump could induce a strong change, and especially how the sign of the transverse strain would depend on the initial magnetization direction in the iron film.

**Simulations and fitting.** To properly model our X-ray diffraction experiment, the continuum model of the ultrafast Einstein–De Haas effect needs to be discretized on the atomic scale. The starting point for the lattice-dynamics part of the atomistic simulation is a Born–von Kármán fifth-nearest-neighbour (five-shell) general force-constant model with empirical parameters taken from ref. 26. In Extended Data Table 1, we reproduce their notation for the force-constant matrices originally taken from ref. 44 and described, for example, in ref. 45. For our thin-film calculation, the three-dimensional model of harmonic springs can be reduced to a chain of layers because there are no differential forces between atoms of the same layer. In the following, we assume the experimental situation—that is, a body-centred cubic (bcc) Fe thin-film sample with crystallographic surface (0 0 1), whose magnetization lies completely on the film plane. This film orientation and geometry makes sure that the off-diagonal elements in Extended Data Table 1 do not contribute to the lattice dynamics. We call the two in-plane directions  $x$  and  $y$  and the out-of-plane direction, which is the direction of the chain,  $z$ . Both the compressive (longitudinal) and the shear (transverse) strain waves travel along the  $z$  direction.

The fundamental units of this reduced model are layers of thickness  $\frac{1}{2}a$ , where  $a = 2.860 \text{ \AA}$  is the lattice constant<sup>46</sup> of bcc Fe. The independent dynamic coordinates of each layer  $N$  are the displacements from the equilibrium position,  $\epsilon_N = (\epsilon_{xN}, \epsilon_{yN}, \epsilon_{zN})$ . As stated above, no relative movement of the atoms within one layer is needed, because all forces—both external and internal—are identical for atoms of the same layer. The equation of motion for layer  $N$  can thus be written as

$$m_N \frac{d^2}{dt^2} \epsilon_N = \sum_{\substack{n=-\Delta N \\ (N+n) \in [N_{\min}, N_{\max}]}}^{\Delta N} \sum_{j=x,y,z} k_{jn} \epsilon_{j(N+n)} \hat{e}_j \quad (8)$$

where  $m_N$  is the mass of the  $N$ th layer and  $\hat{e}_j$  is a Cartesian unit vector. The number  $\Delta N$  of neighbouring layers that are taken into account and the spring constants  $k_{N \pm \Delta N}$  are determined from the three-dimensional model. For the fifth-neighbour iron model we find  $\Delta N = 3$ , and the effective spring constants for the layers are as follows (see Extended Data Table 2)

$$k_{x \pm 3} = k_{y \pm 3} = 4\beta_4 \quad (9)$$

$$k_{z \pm 3} = 4\alpha_4 \quad (10)$$

$$k_{x \pm 2} = k_{y \pm 2} = \beta_2 + 2\alpha_3 + 4\alpha_5 \quad (11)$$

$$k_{z \pm 2} = \alpha_2 + 4\beta_3 + 4\alpha_5 \quad (12)$$

$$k_{x \pm 1} = k_{y \pm 1} = 4\alpha_1 + 4\alpha_4 + 4\beta_4 \quad (13)$$

$$k_{z \pm 1} = 4\alpha_1 + 8\beta_4 \quad (14)$$

For the compressive wave, we used the absorbed fluence of the iron film and the heat capacity of bcc Fe compiled in ref. 47 to calculate the temperature increase from the laser pump. The result is a final temperature of 651 K when starting at 200 K. The effective thermal stress is then estimated from literature values for the linear thermal expansion coefficient of iron<sup>48</sup> and the elastic constants<sup>49</sup>. Because our pump–probe delay times are much smaller than the time needed for acoustic

waves to propagate from the lateral edges of the pumped area to the probed region (about 100 ns for our geometry), we can treat the wave as quasi-one-dimensional<sup>50</sup>.

For the transverse wave, the density<sup>46,51</sup> and saturation magnetization<sup>52</sup> of bcc iron were taken from the literature (for films thicker than 10 nm, bulk values are appropriate<sup>53</sup>), and we then discretized the spatial gradient of the initial magnetization. Because the shape of the gradient is not known precisely, there is seemingly a bit of freedom here: in one extreme, all layers of the film initially have the same magnetization, right up to the surface layer, with the magnetization dropping to zero right at the surface, over less than one unit cell. One could also imagine that the initial magnetization decreases more smoothly over a few layers close to the surface. We modelled the demagnetization-induced lattice dynamics for different initial cases, from a half-unit-cell sharp drop at the surface to a gradual decrease over the top 10 monolayers. Although the detailed shape of the strain wave in the lattice dynamics model is slightly different, once the X-ray diffraction signal in the region of interest is calculated (that is, in the  $(2\ 2\ L)$  CTR, with  $L$  between 0.03 and 0.1), all cases are virtually indistinguishable. This makes sense because an out-of-plane component of the momentum transfer of up to 0.1 reciprocal lattice units implies that the spatial resolution in the out-of-plane direction cannot be better than about 10 monolayers.

The substrate and the capping layers of the film were treated in the model by modifying the masses of the respective parts of the linear chain so that they gave the correct volumetric density of the respective material (MgAl<sub>2</sub>O<sub>4</sub>, MgO, Al). In a second step, the spring constants inside those layers were all scaled so that the correct longitudinal speed of sound for the material was reproduced. At the interfaces between dissimilar materials, the averages of the spring constants on both sides were taken. This procedure leads to the correct amount of reflection and transmission of the strain wave at the interface with the substrate, and the capping layers are fairly thin and light, such that small details of the propagation inside them do not lead to a strong effect on the dynamics in the iron film, which is what the diffraction experiment is sensitive to. Example snapshots of the transverse components of the displacement, strain and velocity are shown in Extended Data Fig. 4 for various times as a function of depth  $z$ . The transverse velocity profile in the displacement and velocity fields is, to leading order, related to the mechanical component of the angular momentum in the probed volume via  $L_{\text{mech}} = A \int z \rho v_{\perp} dz$ , where  $\rho$  is the material density and  $A$  is the effective area of the probe. In the last step of the simulation, the calculated real-space trajectories in all the iron layers considered in the simulation were mapped to the expected X-ray diffraction signal in the  $(2\ 2\ L)$  truncation rod using a simple kinematic diffraction model with extinction.

The multi-step simulation procedure of lattice dynamics and X-ray diffraction cannot directly be fitted to the measured data. Instead, we calculated the expected magnetic difference signal for different discrete settings of the angular momentum transfer time to the lattice (modelled by an exponential response function with a time constant of 0, 10, 25, 50, 100, 250, 500, 1,000 and 2,500 fs and in the range 100–400 fs in 20-fs steps) and of the magnitude (angular momentum corresponding to 0%–30% of the saturation magnetization, in 1% steps). The magnetic difference signal of each simulation run, normalized per  $q_z$  band to the intensity before time zero and corrected for the Debye–Waller drop, was compared to the experimental data and the goodness of fit was assessed with the  $\chi^2$  measure. Only  $q_z$  slices with sufficient signal-to-noise ratio were included. The best  $\chi^2$  value was found at 200 fs and at a demagnetization of 8% of the saturation magnetization (which corresponds to 80% of the demagnetization seen by MOKE, which was 10% under the same conditions). The full  $\chi^2$  maps for both time ranges are displayed in Extended Data Fig. 3.

For the simulation-independent extraction of the frequencies in Fig. 3, the experimental data were binned into  $q_z$  slices. The initial drop was removed and the remaining curvature of the trace was corrected with a quadratic background subtraction. The frequencies were extracted by fast Fourier transforms (FFT) using zero padding and a Chebychev window with width set to the length of the unpadded data. Lastly, a Gaussian fit was used to extract the main frequency component of the FFT. The width of the Gaussian was constrained to less than 0.7 THz to correctly find the acoustic peak and avoid fitting extremely wide peaks at very high frequencies, where the transverse data are most noisy. This processing chain, optimized for the experimental data, was kept unchanged for the simulated data as verification.

In Fig. 2, the error bars for the noise-free simulated data are the asymptotic errors from the Gaussian fits to the peaks in the FFT spectra of the  $q_z$  bands. We then performed a single weighted fit to the linear dispersion function  $\omega = vq_z$  to extract the sound velocity; the uncertainties for the simulations are the asymptotic errors of this fit. For the experimental data we performed a bootstrapping procedure to estimate the uncertainties in the dispersion slopes. For the bootstrapping, we took as a starting point the measured time traces, integrated over the selected ranges of momentum transfer. We then constructed 1,000 virtual datasets by adding Gaussian-distributed noise to each data point, with a  $1\sigma$  width equal to the standard error of each point, as determined from 158 real independent scans. We

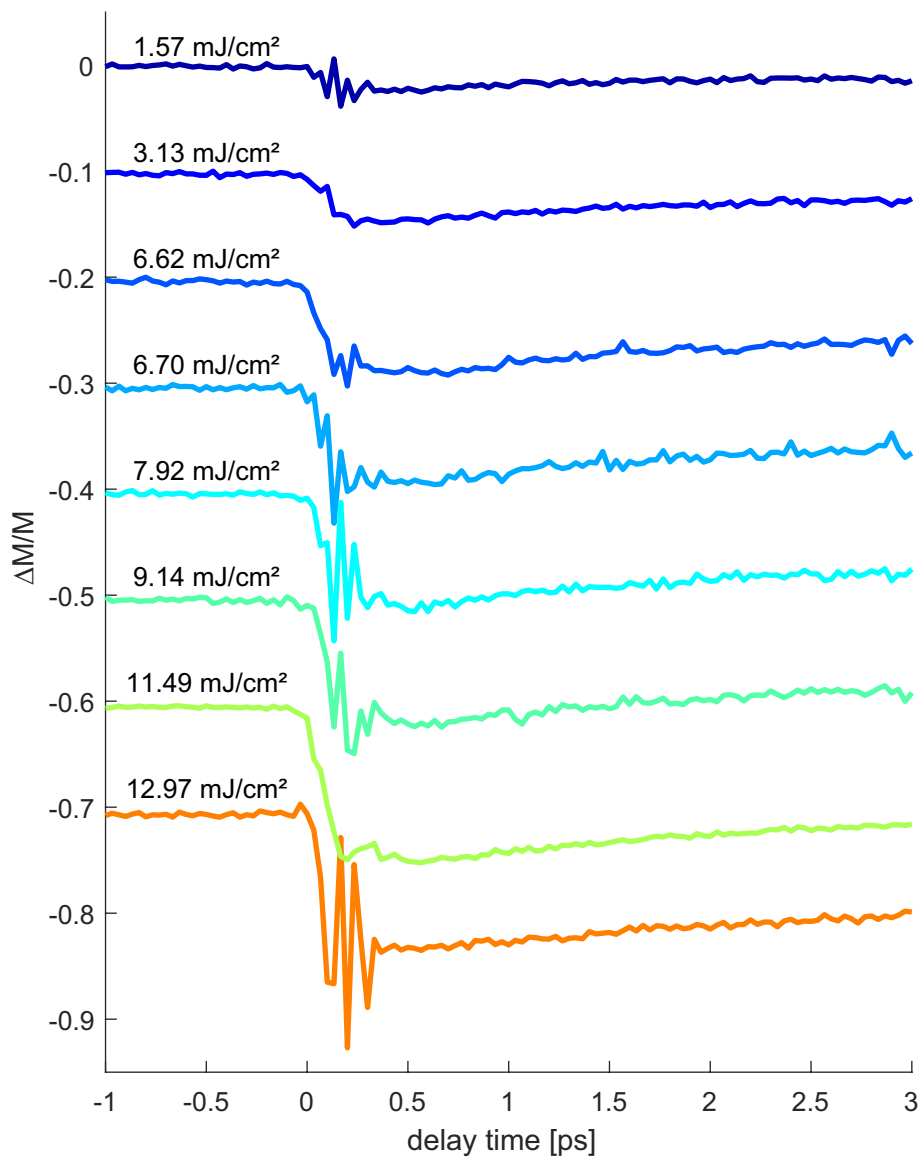
then performed the same analysis procedure as for the simulated data on each of these virtual datasets to get a distribution of results for the speed of sound. Both distributions for the speed of sound show a nearly Gaussian-shaped profile, although the difference measurements have a long, but very small, asymmetric tail extending to higher frequencies. We estimated the most probable value and the uncertainties in these distributions by fitting them with a Gaussian profile and report the mean value with uncertainties corresponding to  $1\sigma$  of the fitted Gaussian shape.

**Code availability.** Data processing and simulation codes are available from the corresponding author on reasonable request.

### Data availability

Raw data were generated at the LCLS large-scale facility, and intermediate datasets were generated during analysis. The raw and intermediate datasets are available from the corresponding author on reasonable request.

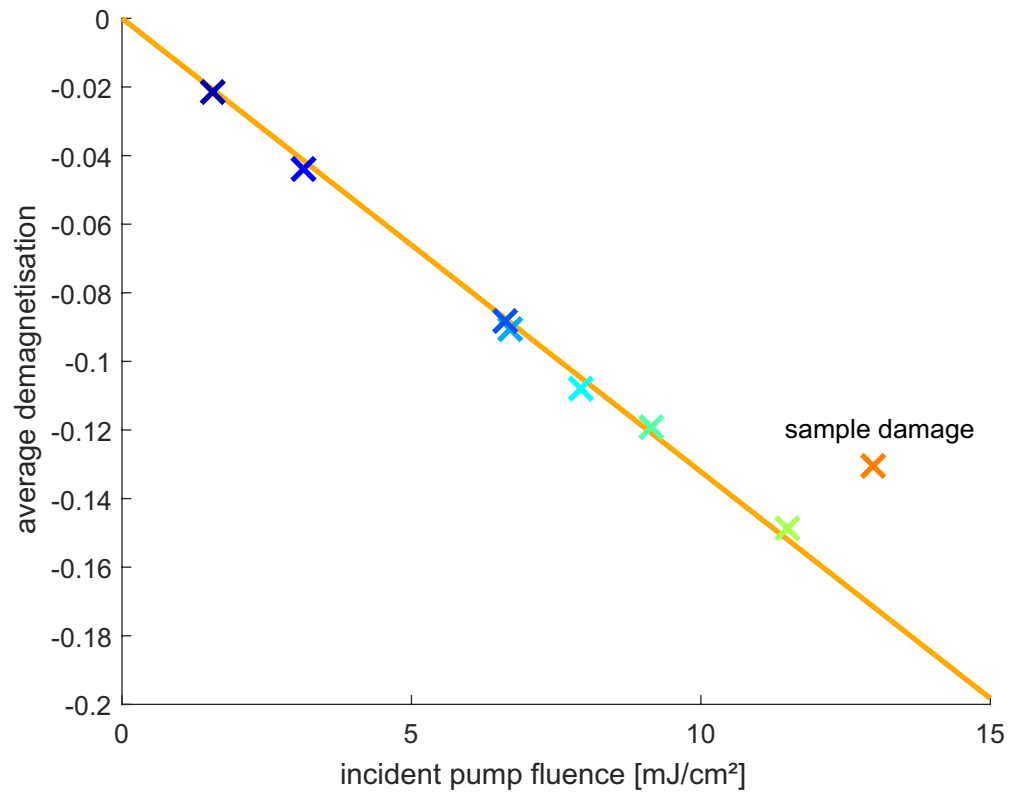
31. Lebedev, M. V., Misochko, O. V., Dekorsy, T. & Georgiev, N. On the nature of “coherent artifact”. *J. Exp. Theor. Phys.* **100**, 272–282 (2005).
32. Radu, I. et al. Laser-induced magnetization dynamics of lanthanide-doped permalloy thin films. *Phys. Rev. Lett.* **102**, 117201 (2009).
33. Marklund, K. & Mahmoud, S. A. Elastic constants of magnesium oxide. *Phys. Scr.* **3**, 75–76 (1971).
34. Villars, P. (ed.) *Al sound velocity. Pauling file in Inorganic Solid Phases, SpringerMaterials (online database)* (Springer, Heidelberg, 2016); available at [https://materials.springer.com/isp/physical-property/docs/ppp\\_003614](https://materials.springer.com/isp/physical-property/docs/ppp_003614).
35. Chollet, M. et al. The X-ray Pump–Probe instrument at the Linac Coherent Light Source. *J. Synchrotron Radiat.* **22**, 503–507 (2015).
36. Fognini, A. et al. Magnetic pulser and sample holder for time- and spin-resolved photoemission spectroscopy on magnetic materials. *Rev. Sci. Instr.* **83**, 063906 (2012).
37. Bionta, M. R. et al. Spectral encoding method for measuring the relative arrival time between X-ray/optical pulses. *Rev. Sci. Instr.* **85**, 083116 (2014).
38. Herrmann, S. et al. CSPAD-140k: a versatile detector for LCLS experiments. *Nucl. Instr. Meth. A* **718**, 550–553 (2013).
39. Born, M. & Wolf, E. *Principles of Optics Electromagnetic Theory of Propagation, Interference and Diffraction of Light* 7th edn (Cambridge Univ. Press, Cambridge, 1999).
40. Palik, E. *Handbook of Optical Constants of Solids* (Academic Press, San Diego, 1991).
41. Ordal, M. A., Bell, R. J., Alexander, R. W., Newquist, L. A. & Querry, M. R. Optical properties of Al, Fe, Ti, Ta, W, and Mo at submillimeter wavelengths. *Appl. Opt.* **27**, 1203–1209 (1988).
42. Lai, W., Rubin, D., Krempel, E. & Rubin, D. *Introduction to Continuum Mechanics* (Butterworth-Heinemann, Burlington, 2009).
43. Pezeril, T., Leon, F., Chateigner, D., Kooi, S. & Nelson, K. A. Picosecond photoexcitation of acoustic waves in locally canted gold films. *Appl. Phys. Lett.* **92**, 061908 (2008).
44. Woods, A. *Inelastic Scattering of Neutrons in Solids and Liquids* Vol. 2, 3 (International Atomic Energy Agency, Vienna, 1963).
45. Flocken, J. W. & Hardy, J. R. Application of the method of lattice statics to vacancies in Na, K, Rb, and Cs. *Phys. Rev.* **177**, 1054–1062 (1969).
46. Sutton, A. & Hume-Rothery, W. The lattice spacings of solid solutions of titanium, vanadium, chromium, manganese, cobalt and nickel in  $\alpha$ -iron. *Lond. Edinb. Dubl. Phil. Mag.* **46**, 1295–1309 (1955).
47. Dinsdale, A. SGTE data for pure elements. *Calphad* **15**, 317–425 (1991).
48. Nix, F. C. & MacNair, D. The thermal expansion of pure metals: copper, gold, aluminum, nickel, and iron. *Phys. Rev.* **60**, 597–605 (1941).
49. Adams, J. J., Agosta, D. S., Leisure, R. G. & Ledbetter, H. Elastic constants of monocrystal iron from 3 to 500 K. *J. Appl. Phys.* **100**, 113530 (2006).
50. Lindenberg, A. M. *Ultrafast Lattice Dynamics in Solids Probed by Time-resolved X-ray Diffraction*. PhD thesis, Univ. California, Berkeley (2001).
51. Meija, J. et al. Atomic weights of the elements 2013 (IUPAC technical report). *Pure Appl. Chem.* **88**, 265–291 (2016).
52. Crangle, J. & Goodman, G. M. The magnetization of pure iron and nickel. *Proc. Royal Soc. Lond. A* **321**, 477–491 (1971).
53. Vaz, C. A. F., Bland, J. A. C. & Lauhoff, G. Magnetism in ultrathin film structures. *Rep. Progr. Phys.* **71**, 056501 (2008).



**Extended Data Fig. 1 | Optical pump–probe measurements of the sample magnetization at varying incident fluence.** The individual traces have been offset for clarity. These results were taken by recreating the geometric conditions of the X-ray experiment, that is, the laser spot

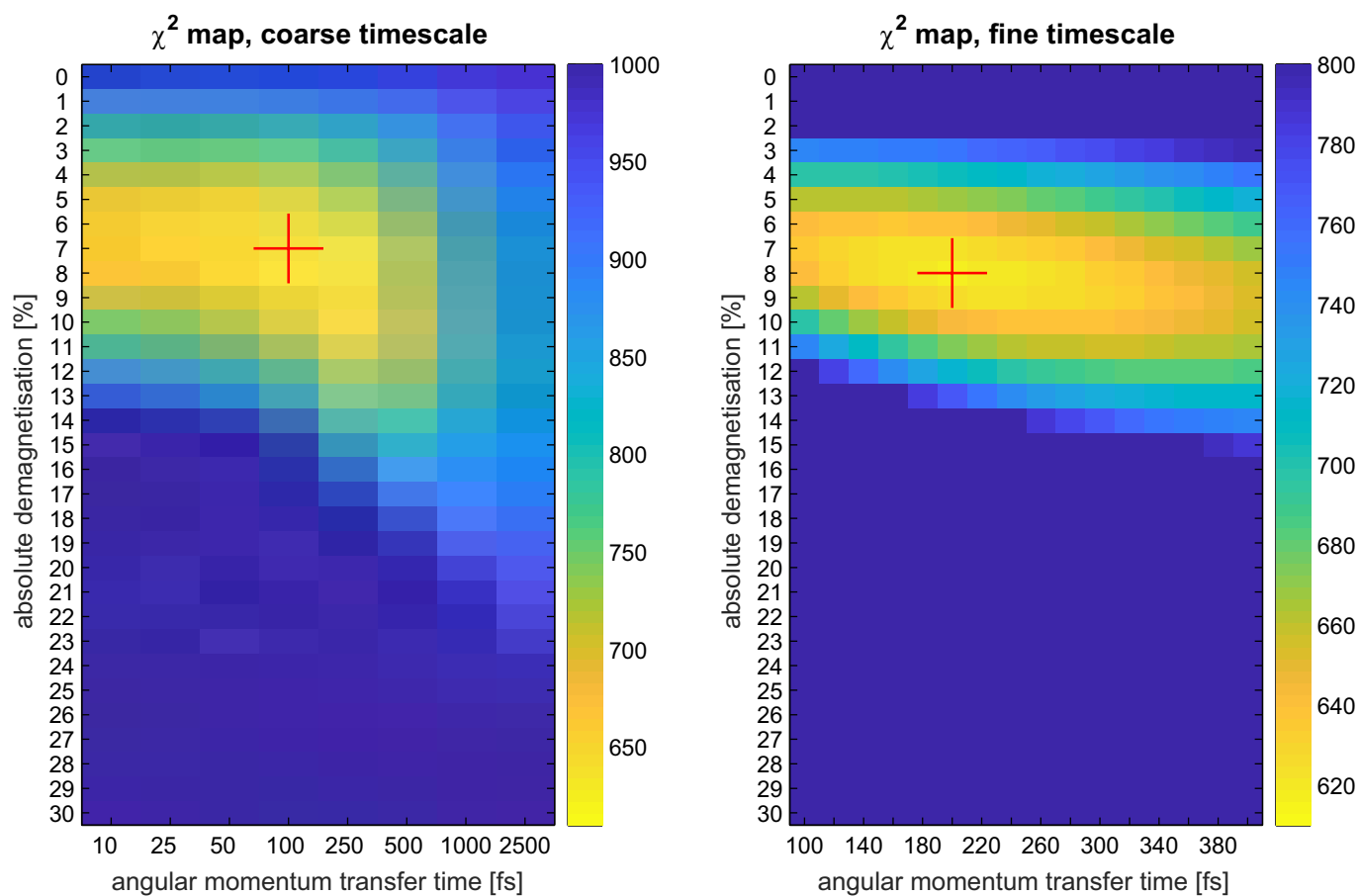
size and angle of incidence were identical. At the highest fluence, laser damage was evident, and the static MOKE signal of the damaged area was permanently lower afterwards.





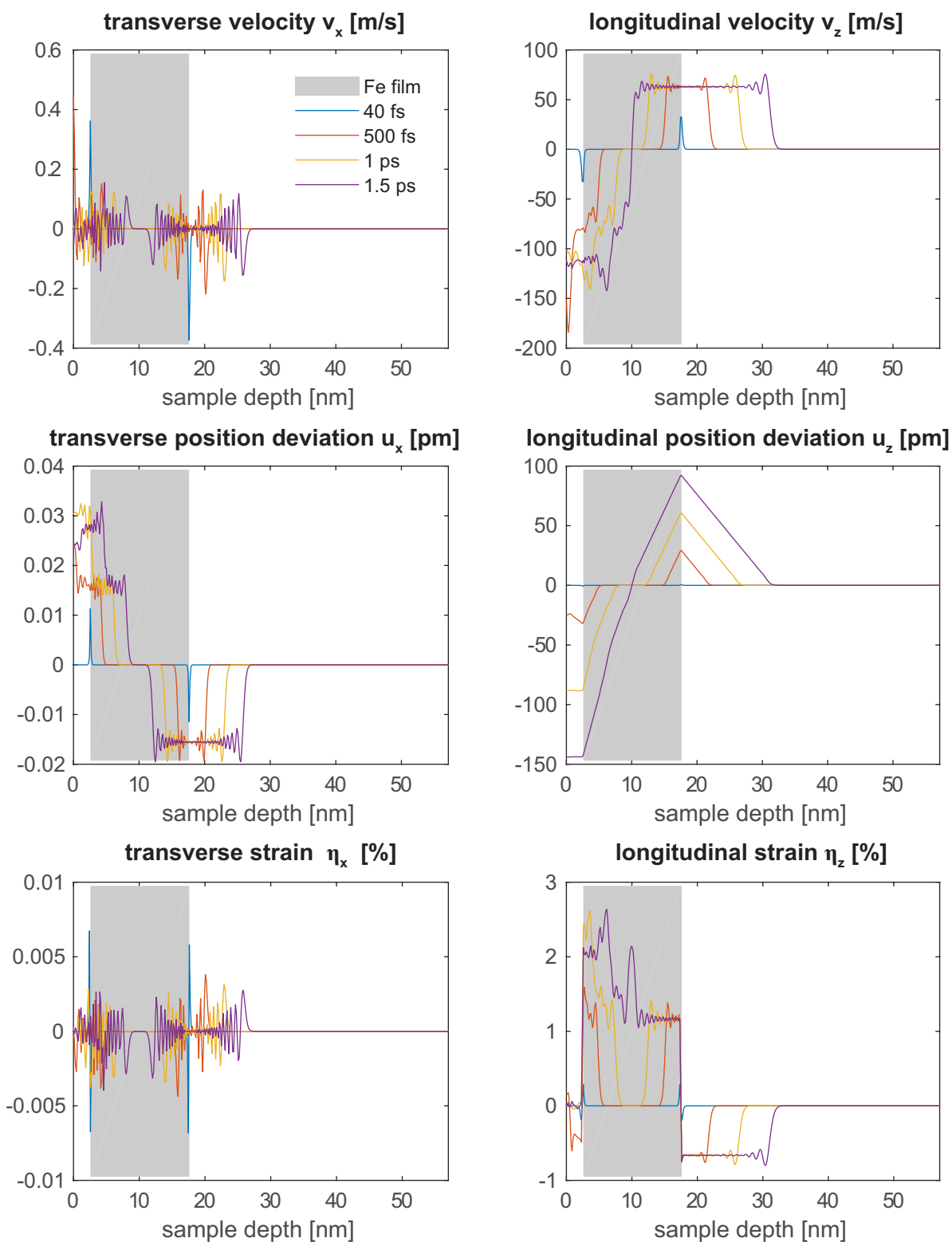
**Extended Data Fig. 2 | Maximum relative demagnetization as a function of fluence.** From the traces in Extended Data Fig. 1, the magnitudes of demagnetization just after the coherent artefact (0.4–0.7 ps) were extracted. A linear fit (excluding the highest fluence where damage was

evident) captures the observed behaviour well. The fluence in the X-ray experiment was  $8.0 \pm 0.3 \text{ mJ cm}^{-2}$ , corresponding to a demagnetization of 10%.

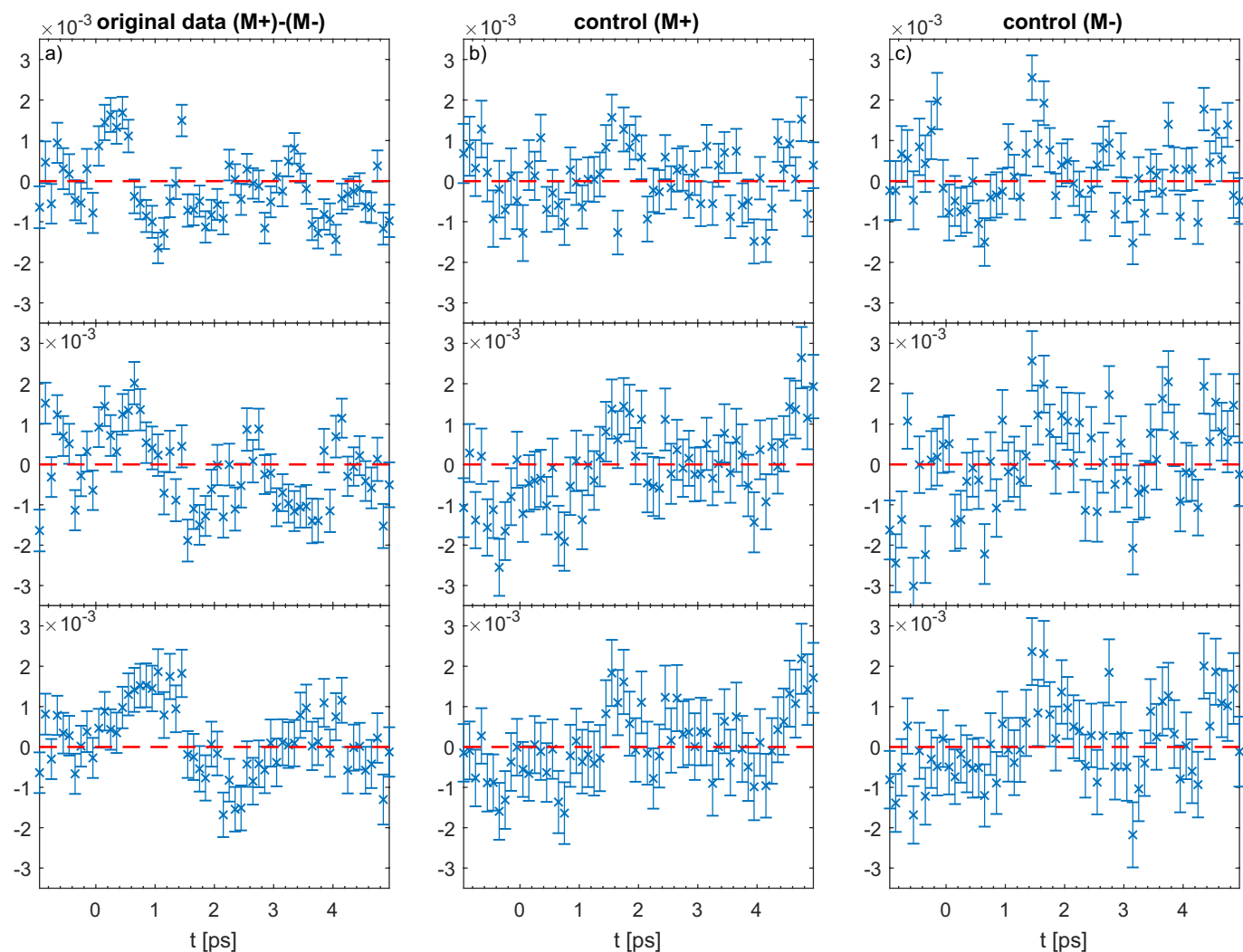


**Extended Data Fig. 3 | Goodness of fit, assessed by  $\chi^2$ , for different combinations of angular momentum transfer time and magnitude.** The left panel has a coarse logarithmic axis for the transfer time, whereas the right panel has a linear scale for a more precise determination of the optimum. The optima are indicated by the red crosses; for the coarse

scale, the best  $\chi^2$  of 628.9 is reached for the simulation with 100 fs transfer time and 7% magnitude. For the fine scale, the best values are 200 fs and 8%, with a  $\chi^2$  of 618.8. The traces in Fig. 2 were generated using the latter parameters.



**Extended Data Fig. 4 | Snapshots of simulated velocity, displacement and strain in the transverse and longitudinal direction at different times.** The iron film is indicated by grey shading; to the left are the Al and MgO capping layers and to the right is the  $\text{MgAl}_2\text{O}_4$  substrate.



**Extended Data Fig. 5 | Magnetic difference signal plots and two ‘virtual’ control measurements with the same magnetization sign.** The three vertical panels of each set show the three  $q_z$  ranges centred at 0.0737, 0.0482 and 0.0236 reciprocal lattice units, as in Fig. 2. We constructed the ‘M+’ virtual control dataset by taking only the  $M > 0$  data from each of the 158 scans. Data analysis was then performed by taking the difference of all even and all odd scan numbers. The ‘M-’ control dataset was created

in the same manner by using only the  $M < 0$  shots. We note that the uncertainties on both control sets are larger than for the actual magnetic difference data, because each control set uses only half of the total data. These control measurements are also more strongly influenced by longer-term drifts in the alignment of the free electron laser (there were about 4 min between consecutive scans), leading to some noise correlations. Nevertheless, all control sets are consistent with no signal.

**Extended Data Table 1 | Force-constant matrices for bcc metals in the five-shell Born-von Kármán model**

Atom position	Force constant matrix	<i>bcc</i> Fe, 300K
$\frac{a}{2}(1, 1, 1)$	$\begin{pmatrix} \alpha_1 & \beta_1 & \beta_1 \\ \beta_1 & \alpha_1 & \beta_1 \\ \beta_1 & \beta_1 & \alpha_1 \end{pmatrix}$	$\alpha_1 = 16.88 \frac{\text{N}}{\text{m}}$ $\beta_1 = 15.01 \frac{\text{N}}{\text{m}}$
$\frac{a}{2}(2, 0, 0)$	$\begin{pmatrix} \alpha_2 & 0 & 0 \\ 0 & \beta_2 & 0 \\ 0 & 0 & \beta_2 \end{pmatrix}$	$\alpha_2 = 14.63 \frac{\text{N}}{\text{m}}$ $\beta_2 = 0.55 \frac{\text{N}}{\text{m}}$
$\frac{a}{2}(2, 2, 0)$	$\begin{pmatrix} \alpha_3 & \gamma_3 & 0 \\ \gamma_3 & \alpha_3 & 0 \\ 0 & 0 & \beta_3 \end{pmatrix}$	$\alpha_3 = 0.92 \frac{\text{N}}{\text{m}}$ $\beta_3 = -0.57 \frac{\text{N}}{\text{m}}$ $\gamma_3 = 0.69 \frac{\text{N}}{\text{m}}$
$\frac{a}{2}(3, 1, 1)$	$\begin{pmatrix} \alpha_4 & \delta_4 & \delta_4 \\ \delta_4 & \beta_4 & \gamma_4 \\ \delta_4 & \gamma_4 & \beta_4 \end{pmatrix}$	$\alpha_4 = -0.12 \frac{\text{N}}{\text{m}}$ $\beta_4 = 0.03 \frac{\text{N}}{\text{m}}$ $\gamma_4 = 0.52 \frac{\text{N}}{\text{m}}$ $\delta_4 = 0.007 \frac{\text{N}}{\text{m}}$
$\frac{a}{2}(2, 2, 2)$	$\begin{pmatrix} \alpha_5 & \beta_5 & \beta_5 \\ \beta_5 & \alpha_5 & \beta_5 \\ \beta_5 & \beta_5 & \alpha_5 \end{pmatrix}$	$\alpha_5 = -0.29 \frac{\text{N}}{\text{m}}$ $\beta_5 = 0.32 \frac{\text{N}}{\text{m}}$

The values in the right column are from ref. <sup>26</sup>. The notation is reproduced from ref. <sup>45</sup>.

**Extended Data Table 2 | Force-constant contributions for a chain of layers along  $z$** 

Neighbour class	Specific neighbours	In layer	# of atoms	$k_x$	$k_y$	$k_z$
(1,1,1)	$(\pm 1, \pm 1, 1)$	$N + 1$	4	$\alpha_1$	$\alpha_1$	$\alpha_1$
	$(\pm 1, \pm 1, -1)$	$N - 1$	4	$\alpha_1$	$\alpha_1$	$\alpha_1$
(2,0,0)	$(0, 0, 2)$	$N + 2$	1	$\beta_2$	$\beta_2$	$\alpha_2$
	$(\pm 2, 0, 0)$	$N$	2	$\alpha_2$	$\beta_2$	$\beta_2$
	$(0, \pm 2, 0)$	$N$	2	$\beta_2$	$\alpha_2$	$\beta_2$
	$(0, 0, -2)$	$N - 2$	1	$\beta_2$	$\beta_2$	$\alpha_2$
(2,2,0)	$(\pm 2, 0, 2)$	$N + 2$	2	$\alpha_3$	$\beta_3$	$\alpha_3$
	$(0, \pm 2, 2)$	$N + 2$	2	$\beta_3$	$\alpha_3$	$\alpha_3$
	$(\pm 2, \pm 2, 0)$	$N$	4	$\alpha_3$	$\alpha_3$	$\beta_3$
	$(\pm 2, 0, -2)$	$N - 2$	2	$\alpha_3$	$\beta_3$	$\alpha_3$
	$(0, \pm 2, -2)$	$N - 2$	2	$\beta_3$	$\alpha_3$	$\alpha_3$
(3,1,1)	$(\pm 1, \pm 1, 3)$	$N + 3$	4	$\beta_4$	$\beta_4$	$\alpha_4$
	$(\pm 3, \pm 1, 1)$	$N + 1$	4	$\alpha_4$	$\beta_4$	$\beta_4$
	$(\pm 1, \pm 3, 1)$	$N + 1$	4	$\beta_4$	$\alpha_4$	$\beta_4$
	$(\pm 3, \pm 1, -1)$	$N - 1$	4	$\alpha_4$	$\beta_4$	$\beta_4$
	$(\pm 1, \pm 3, -1)$	$N - 1$	4	$\beta_4$	$\alpha_4$	$\beta_4$
	$(\pm 1, \pm 1, -3)$	$N - 3$	4	$\beta_4$	$\beta_4$	$\alpha_4$
(2,2,2)	$(\pm 2, \pm 2, 2)$	$N + 2$	4	$\alpha_5$	$\alpha_5$	$\alpha_5$
	$(\pm 2, \pm 2, -2)$	$N - 2$	4	$\alpha_5$	$\alpha_5$	$\alpha_5$

The classes of neighbouring atoms, as well as their multiplicities and contributions to the force constants between layers, are given for the principal directions.